

Article

Improved InGaAs and InGaAs/InAlAs Photoconductive Antennas Based on (111)-Oriented Substrates

Kirill Kuznetsov ^{1,*} , Aleksey Klochkov ^{2,*}, Andrey Leontyev ¹, Evgeniy Klimov ², Sergey Pushkarev ², Galib Galiev ² and Galiya Kitaeva ¹ 

¹ Faculty of Physics, Lomonosov Moscow State University, Moscow 119991, Russia; aa.leontjev@physics.msu.ru (A.L.); gkitaeva@physics.msu.ru (G.K.)

² V.G. Mokerov Institute of Ultra High Frequency Semiconductor Electronics of Russian Academy of Sciences, Moscow 117105, Russia; klimov_evgeniy@mail.ru (E.K.); s_s_e_r_p@mail.ru (S.P.); galiev_galib@mail.ru (G.G.)

* Correspondence: kirill-spdc@yandex.ru (K.K.); klochkov_alexey@mail.ru (A.K.)

Received: 28 February 2020; Accepted: 14 March 2020; Published: 17 March 2020



Abstract: The terahertz wave generation by spiral photoconductive antennas fabricated on low-temperature In_{0.5}Ga_{0.5}As films and In_{0.5}Ga_{0.5}As/In_{0.5}Al_{0.5}As superlattices is studied by the terahertz time-domain spectroscopy method. The structures were obtained by molecular beam epitaxy on GaAs and InP substrates with surface crystallographic orientations of (100) and (111)A. The pump-probe measurements in the transmission geometry and Hall effect measurements are used to characterize the properties of LT-InGaAs and LT-InGaAs/InAlAs structures. It is found that the terahertz radiation power is almost four times higher for LT-InGaAs samples with the (111)A substrate orientation as compared to (100). Adding of LT-InAlAs layers into the structure with (111)A substrate orientation results in two orders of magnitude increase of the structure resistivity. The possibility of creating LT-InGaAs/InAlAs-based photoconductive antennas with high dark resistance without compensating Be doping is demonstrated.

Keywords: terahertz wave generation; InGaAs; molecular beam epitaxy; time-domain spectroscopy; photoconductive antenna

1. Introduction

At the present time terahertz wave radiation is widely used in various application fields related to pharmacology, medicine, security systems, and data transmission. Therefore, a search is underway for the most effective methods for generating and detecting terahertz radiation. In this regard, photoconductive semiconductor antennas (PCAs) have proven themselves as flexible and effective THz devices for use in time-domain spectroscopy (TDS) and imaging systems. Due to the availability of cost-efficient and reliable components from the telecommunication industry, the state-of-the-art TDS systems often utilize optical excitation at 1550 nm [1,2] with Er³⁺ fiber laser femtosecond pulses. Recently [3,4], the In_{0.5}Ga_{0.5}As-based semiconductor structures have been investigated as photoconductive materials for THz PCAs due to an appropriate room-temperature optical absorption cut-off wavelength of 1.5 μm. Lately, a significant improvement in the performance of these devices was achieved, mainly with the help of nanotechnology tools such as plasmonic light concentrators, plasmonic contact electrodes, optical nanoantenna arrays, or optical nanocavities [5–7]. Nevertheless, the development of basic photoconductive materials for THz PCAs is still of current interest.

In order to generate fast transient current and to sample the THz pulse accurately in the time domain, THz PCAs require a photoconductor with high dark resistivity and a short carrier lifetime after

optical excitation. Additionally, high electron mobility is necessary for THz PCA detectors. The main development challenge with InGaAs-based photoconductors is relatively small bandgap resulting in low breakdown field strength and large dark background conductivity. Several methods for producing ultrafast InGaAs photoconductive structures have been proposed: ion implantation with heavy ions followed by thermal annealing treatment [8,9], epitaxial doping of InGaAs with impurities producing deep electronic traps in the bandgap [10,11], and growth of specially designed heterostructures such as ErAs inclusions in InGaAlAs [12]. The low-temperature (LT) InGaAs-based epitaxial structures are widely used in commercial THz systems. Low substrate temperatures ($T_G \approx 200$ °C) lead to non-stoichiometric growth with the incorporation of excess arsenic in the crystal structure. The most common non-stoichiometry related point defect is arsenic antisite with concentration in the range of 10^{17} – 10^{19} cm^{-3} depending on the substrate temperature and arsenic overpressure [13–15]. The fast capture of photogenerated electrons and recombination with holes through antisite centers results in sub-picosecond carrier lifetimes in LT-materials at optimized growth and annealing conditions [16]. LT-InGaAs shows a high room-temperature residual electron concentration of the order of 10^{17} cm^{-3} due to the thermal ionization of antisite defects. To increase the structure resistivity, LT-InAlAs layers are added to the photoconductive material. LT-InAlAs layers have a higher dark resistivity as compared to LT-InGaAs and exhibit deep trap states that are situated energetically below the antisite defect levels of adjacent InGaAs layers. With acceptor doping by beryllium (Be) atoms, LT-InGaAs/InAlAs superlattices demonstrate both low residual electron concentration and short carrier lifetimes in the sub-picosecond range [17–19].

It was shown recently [20–22] that LT-InGaAs and LT-GaAs structures, fabricated on (n11)A-oriented GaAs or InP substrates with or without PCA electrodes, under pulsed laser excitation, can generate THz radiation with higher power as compared to structures obtained on conventional (100) substrates. It was argued that substrate orientation can influence the concentration and the type of defects in low-temperature grown films. The purpose of the present work is further clarification of the nature of this effect by investigating the carrier dynamics in LT-InGaAs-based epitaxial structures grown on (111)A GaAs and InP substrates. Among the structures, for the first time we study the PCA based on LT-InGaAs/InAlAs superlattice fabricated on InP (111)A-oriented substrate.

2. Materials and Methods

Figure 1 shows the schematic of photoconductive terahertz source, which consists of a spiral antenna fabricated on an epitaxial heterostructure. As the photoconductive heterostructures we investigate undoped $\text{In}_{0.53}\text{Ga}_{0.47}\text{As}$ layers with metamorphic buffer on GaAs substrates [20] and an undoped lattice-matched $\text{In}_{0.53}\text{Ga}_{0.47}\text{As}/\text{In}_{0.52}\text{Al}_{0.48}\text{As}$ superlattice on InP substrate. The $\text{In}_{0.53}\text{Ga}_{0.47}\text{As}$ layers serve as the photo-absorbing active regions. The mole fraction of indium is chosen as 0.53 to provide an optical absorption cut-off wavelength close to the operating wavelength of 1.5 μm . The room temperature absorption coefficient for $\text{In}_{0.53}\text{Ga}_{0.47}\text{As}$ layers lattice matched to InP substrates is 8000–12000 cm^{-1} in this wavelength range [23,24]. The thickness of LT- $\text{In}_{0.53}\text{Ga}_{0.47}\text{As}$ layers is chosen as 660 nm to be of the order of the excitation light penetration depth. Also, the $\text{In}_{0.53}\text{Ga}_{0.47}\text{As}$ layer is sufficiently thin to minimize the dark conductivity. The $\text{In}_{0.52}\text{Al}_{0.48}\text{As}$ layers in superlattice structures are used to introduce deep defect states and to reduce residual carrier concentration.

The active layers of the photoconductive structures are grown by molecular-beam epitaxy (MBE) at a low growth temperature of 200 °C. Two types of structure layer designs on different substrate materials and orientations are investigated. The 660-nm-thick $\text{In}_{0.53}\text{Ga}_{0.47}\text{As}$ layers are grown on GaAs substrates with crystallographic orientations (100) and (111)A. The step-graded metamorphic buffer $\text{In}_x\text{Ga}_{1-x}\text{As}$ is used to accommodate the lattice mismatch between the GaAs substrate and the photoconductive layer. The metamorphic buffer consists of eleven 60-nm-thick $\text{In}_x\text{Ga}_{1-x}\text{As}$ layers with indium composition increment of $\Delta x = 0.05$. The substrate temperature during metamorphic buffer growth is stepwise decreased from 390 °C for $\text{In}_{0.05}\text{Ga}_{0.95}\text{As}$ to 320 °C for the topmost $\text{In}_{0.55}\text{Ga}_{0.45}\text{As}$ layer. The beam equivalent pressure (BEP) of arsenic molecules As_4 is 2.0×10^{-5} Torr during growth.

The III/V BEP ratio is 29. The 100-period $\text{In}_{0.53}\text{Ga}_{0.47}\text{As}$ (12 nm)/ $\text{In}_{0.52}\text{Al}_{0.48}\text{As}$ (8 nm) superlattice is epitaxially grown on the InP (111)A substrate. The BEP of As_4 is 1.2×10^{-5} Torr and III/V BEP ratio is 30. The samples were in-situ annealed in the growth chamber for 30 min at 590°C . On the surface of heterostructures the spiral antennas with 320 nm-thick $\text{Ni}/\text{Ge}/\text{Au}/\text{Ni}/\text{Au}$ annealed ohmic electrodes are deposited using standard photolithography. The central photoconductive gap is $20\ \mu\text{m}$. The Hall mobility and density of charge carriers were measured using the Van der Pauw method at room temperature.

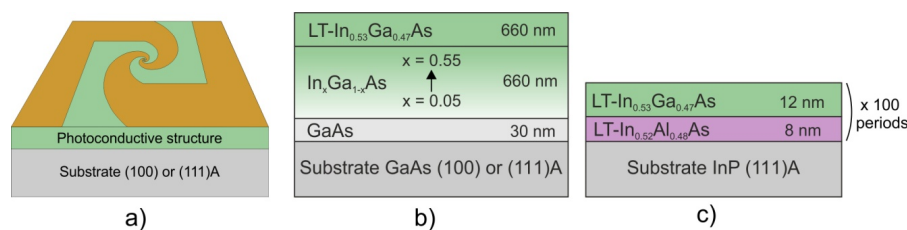


Figure 1. Schematic of the investigated photoconductive semiconductor antenna (PCA) THz emitters: (a) topology of spiral antenna, (b) LT-InGaAs/GaAs (100) and (111)A heterostructures, (c) LT-InGaAs/InAlAs/InP (111)A heterostructure.

One of the most common methods for studying the dynamics of relaxation of charge carriers in semiconductor structures is based on the pump-probe technique. This method has sufficient resolution to observe the dynamics of relaxation of charge carriers on a sub-picosecond time scale [17].

Figure 2 shows our experimental setup for frequency-degenerate pump-probe measurements with time resolution. We measure the temporal behavior of the differential transmission (DT) of the samples induced by pump pulses. The optical radiation source (Las) is a femtosecond Er^{3+} laser (wavelength 1550 nm, pulse duration 100 fs, pulse repetition rate 70 MHz). The initial laser beam was divided into probe and pump beams. The pump and probe beams were separated on a Glan polarization prism (G) and had orthogonal polarizations. The power ratio between the beams was regulated using a $\lambda/2$ plate in front of the Glan prism (G). A pump beam was focused on the sample; it modulated transmittance of the sample due to interband transitions of electrons in a semiconductor film. The time shift between the pulses of pump and probe beams was realized using the corner reflector (C) mounted on the delay line. The shift was changed with the time step $\Delta t = 0.1$ ps. The modulation frequency of the pump radiation chopper (Ch) was chosen equal to 2.3 kHz. The mean pump beam power was 40 mW, the probe beam power was 5 mW. The focal length of the lens (L), which focused the both beams on the sample (S), was $f = 1.5$ cm. An InGaAs-detector (D) by Thorlabs was used to measure the probe differential transmittance. The signal from the detector was recorded using a Lock-in Amplifier (Amp).

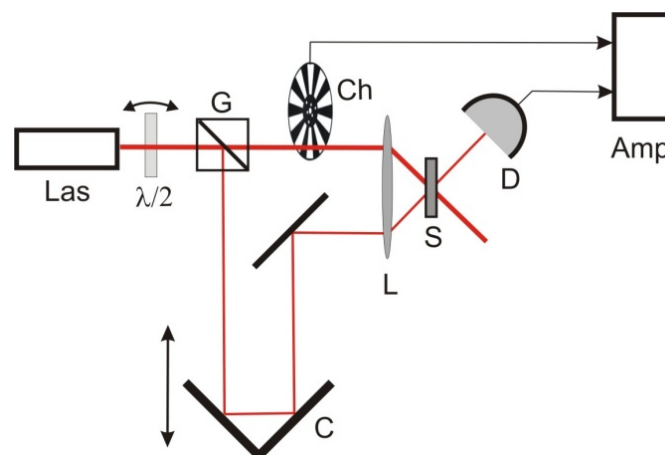


Figure 2. Schematics of the pump-probe setup for frequency-degenerate differential transmission (DT) measurements.

Figure 3 shows the experimental setup for generation and detection of terahertz radiation. The source of optical radiation was the same femtosecond Er^{3+} laser as in pump-probe experiments. After passing through the beam splitter, most of the radiation was directed to a generating photoconductive antenna, and the rest served to illuminate the detector. The pump beam (with a mean power up to 30 mW) was focused by a lens with a focal length of 5 mm onto the studied antennas. For collimation of the generated THz radiation, a matching silicon lens was placed on the output surface of the antenna-generator (PCA1). The refractive index of high-resistive silicon is $n_{\text{Si}} = 3.14$ in the terahertz range. Four parabolic mirrors were used to collect THz radiation and to focus it further on the silicon lens of the antenna-detector (PCA2). The commercial antenna-detector (Menlo Systems) with a symmetrical dipole antenna located on its back surface was used to detect the THz radiation. An instantaneous action of the THz field on an antenna-detector is equivalent to inducing some difference in potentials of its electrodes. However, the corresponding current arises through the antenna only upon irradiation with an optical pulse, which starts the process of generating free charge carriers in a semiconductor wafer. In order to register the temporal dynamics of the THz field, it is necessary to introduce a controlled delay between the pump beam and the probe beam. This is done using a mechanical delay line with a corner reflector installed. Thus, by changing the arrival time of the probe pulse (using a moving delay line), one can measure various instantaneous values of the terahertz field and, thereby, determine its temporal shape of the THz pulse. Detection of the current was performed using a Lock-in Amplifier. For synchronous detection of radiation, a radiation chopper was placed in the optical path, which modulated the laser beam at a frequency $f = 2.3$ kHz.

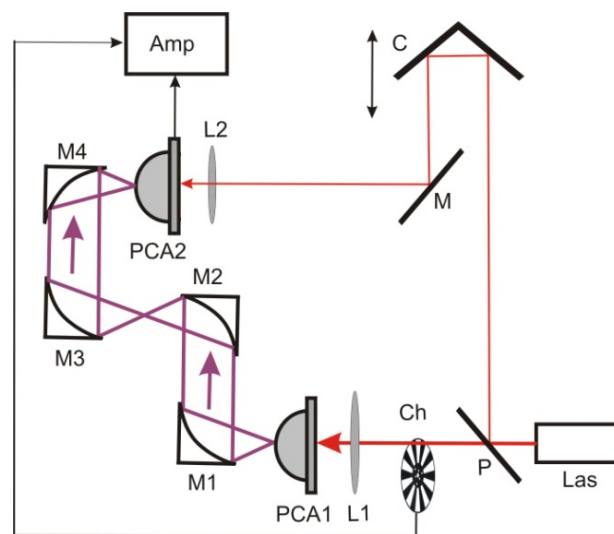


Figure 3. Schematics of the terahertz time-domain spectroscopy setup.

3. Experimental Results

The room-temperature Hall data is presented in Table 1. The electron-type conductivity of the investigated samples is much greater than that of the reference samples of thick undoped $\text{In}_{0.53}\text{Ga}_{0.47}\text{As}$ films lattice-matched to InP (100) substrates obtained at normal growth conditions. The typical unintentional background doping of InGaAs layers in our MBE system is $(1-2) \cdot 10^{15} \text{ cm}^{-3}$. The increase of the electron concentration at low growth temperature of 200°C corresponds to the incorporation of excess As atoms into the InGaAs lattice. The thermal ionization of antisite As defects leads to the free electron volume concentration of the order of 10^{17} cm^{-3} . The electron sheet concentration and mobility depend on the substrate orientation and on the heterostructure design. From the comparison of the LT- InGaAs samples it follows that MBE growth on the (100) and (111) GaAs substrates at identical growth conditions leads to formation of InGaAs layers with different concentration of point defects. It can be concluded that the antisite defect density is greater in the case of

the sample grown on (111)A GaAs substrate. Introduction of InAlAs barrier layers into InGaAs/InAlAs superlattice results in substantial decrease of the sheet electron concentration by an order of magnitude as compared to thick InGaAs layers. The addition of InAlAs layers also leads to reduction of mobility μ . As a result, the dark resistivity of LT-InGaAs/InAlAs (111)A sample is 60 and 130 times greater than that of the LT-InGaAs/GaAs (111)A and (100) samples, correspondingly. The effect of InAlAs layers on the electron transport is associated with the carrier capture by deep traps into InAlAs barriers and with the scattering.

Table 1. Electronic mobility μ and sheet concentration n_s in photoconductive heterostructures.

Sample	n_s (10^{12} cm^{-2})	μ (cm^2/Vs)
LT-InGaAs/GaAs (100)	11.9	380
LT-InGaAs/GaAs (111)A	20.1	110
LT-InGaAs/InAlAs/InP (111)A	1.2	30

The pump-probe measurements were performed for LT-InGaAs samples grown on GaAs substrates with the surface crystallographic orientations of (100) and (111)A and for the LT-InGaAs/InAlAs superlattice grown on an InP substrate with (111)A orientation. Figure 4 shows graphs of the temporal dependences of the normalized transmittance for the studied samples. It should be noted that on some graphs, in the falling part of the functional dependences, there are regions of local growth of the normalized reflection coefficient function. These areas appear due to re-reflection of the signal from the back side of the samples. Points in these areas (dashed rectangles) were cut out of the dependencies for correct subsequent approximation.

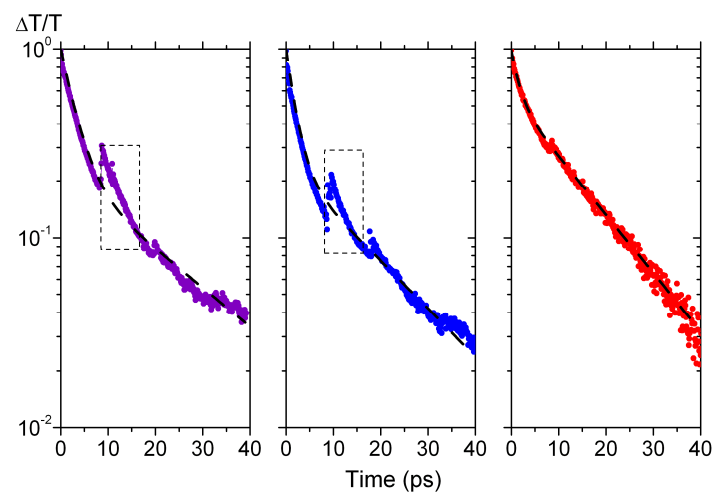


Figure 4. Normalized transmission changes detected for: (left) LT-InGaAs/GaAs(100), (middle) LT-InGaAs/GaAs (111)A, (right) LT-InGaAs/InAlAs/InP (111)A.

Figure 5 shows the temporal profiles of terahertz radiation detected from the studied samples. The measurements were carried out at the same input sensitivity of the Lock-in Amplifier. The magnitude of the applied bias voltage in the case of LT-InGaAs samples was 3.7 V. It can be seen that the signal in the sample grown on a (111)A GaAs substrate is 1.9 times higher than that from the sample grown on (100) GaAs substrate. For the LT-InGaAs / InAlAs (InP) (111)A sample, the applied bias voltage was higher almost by an order of magnitude, equal to 25 V. It can be seen that, mostly due to the higher bias voltage, the signal from the InGaAs / InAlAs-based structure is 5-6 times higher. Applying of higher bias voltage turned out to be possible (without breakdown of the sample) due to significantly higher resistance of this antenna and its lower dark current.

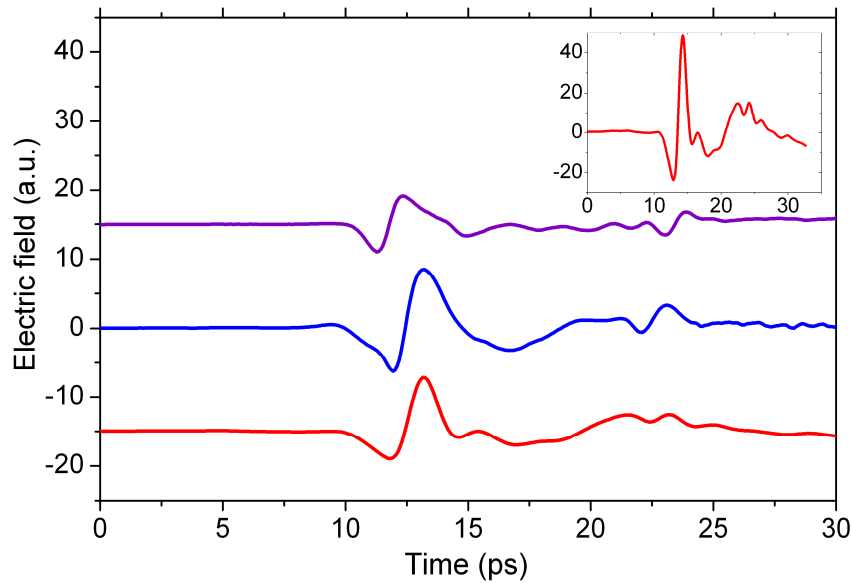


Figure 5. Detected time-domain signal traces: violet line LT-InGaAs/GaAs(100) $U_b = 3.7$ V, blue line LT-InGaAs/GaAs (111)A $U_b = 3.7$ V, red line LT-InGaAs/InAlAs/InP(111)A $U_b = 3.7$ V, (inset) LT-InGaAs/InAlAs/InP(111)A $U_b = 25$ V.

Figure 6 shows the normalized spectra obtained by the fast Fourier transform (FFT) processing of the temporal waveforms presented in Figure 5. It can be seen that the maximum of the power spectral distribution is located at the frequency of 0.2 THz, and the total width of each spectrum is about 2 THz. We have not found significant differences in the spectra of terahertz wave radiation from the studied antennas. Apparently, this is due to the limiting effect of the antenna-detector with an upper frequency of the detection band about 2 THz.

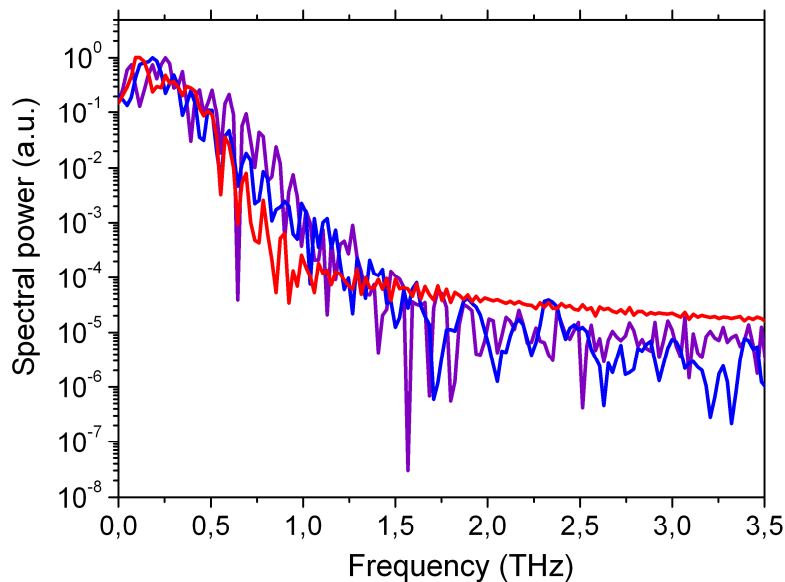


Figure 6. FFT spectra of antennas: violet line LT-InGaAs/GaAs(100), blue line LT-InGaAs/GaAs (111)A, red line LT-InGaAs/InAlAs/InP (111)A.

4. Discussion

4.1. Pump-Probe Results.

Figure 4 shows the experimental temporal dependences of the falling part of the normalized transmittance. Two separated regions (up to 10 ps, after 10 ps) with different slopes of the curve could be clearly distinguished on each of the presented dependencies. Since the curves are plotted on a logarithmic scale, we can assume these regions as two exponential contributions with different characteristic relaxation times. Dependencies are well approximated by a two-exponential decay model. The interpolation was carried out using the least squares method by the following expression:

$$\frac{\Delta T(t)}{T_0} = Ae^{-t/\tau_1} + Be^{-t/\tau_2} \quad (1)$$

Here ΔT is a DT, T_0 is a maximal difference transmission, τ_1 and τ_2 are the relaxation times, A and B are the fitting constants. Fitting results are presented in Table 2.

Table 2. Characteristic relaxation times.

Sample	τ_1 (ps)	τ_2 (ps)
LT-InGaAs/GaAs(100)	3.0 ± 0.1	21.0 ± 0.2
LT-InGaAs/GaAs(111)A	1.9 ± 0.1	17.0 ± 0.3
LT-InGaAs/InAlAs/InP(111)A	1.7 ± 0.1	14.0 ± 0.2

Most likely, the characteristic time τ_1 is the time of an electron capture from the conduction band by an anti-structural defect As_{Ga}^+ . The obtained values of τ_1 are in a good agreement with the data of experiments performed earlier by other scientific groups [2,16,25]. The time interval τ_2 seems to be the recombination time of holes and electrons captured by traps. Its characteristic scale is of the order of tens of picoseconds, which, in order of magnitude, agrees well with the previous experimental values [17]. The origin of the processes that occur with photo-excited electrons at the short capture time τ_1 is connected with the excess of arsenic atoms in the InGaAs crystal structure leading to formation of the special-type defects.

As it is known from the theory by Shockley and Read [26], the carrier capture time by traps (τ_1) is determined by the following expression:

$$\tau_1 = (N_{As^+} v_{th} \sigma_{As^+})^{-1} \quad (2)$$

Here, N_{As^+} is concentration of As+ traps in the crystal, σ_{As^+} is cross-section of the electron capture by traps, and v_{th} is the thermal velocity of electrons. Based on the obtained data, we can conclude that the number of As_{Ga}^+ defects in the LT-InGaAs/GaAs (111)A and LT-InGaAs/InAlAs/InP (111)A samples is almost two times higher than that in LT-InGaAs / GaAs (100).

4.2. Temporal and Spectral Dependences of the Generated THz Field.

Terahertz-wave electric field should be approximately proportional to the derivative of the current density. Indeed, in the simple case of a weak pump, neglecting screening effects, quasi-static and near-field terms in the expression for the electric field, one can obtain the terahertz-wave electric field proportional to the derivative of the concentration of the free electrons [27]. In Figure 5, we see that the terahertz signal amplitude from the sample LT-InGaAs/GaAs (111)A is almost two times higher than that from the sample LT-InGaAs/GaAs (100). This can be explained under the assumption that concentration of charged arsenic traps with (111)A substrate orientation is greater than that with (100) orientation. This assumption is in good agreement with the results of our measurements of characteristic electron capture times. Slower dynamics of charge carriers here could be also explained by decrease in the concentration of active defects As_{Ga}^+ .

It is usually assumed that fast excitation of charge carriers in InGaAs / InAlAs heterostructures occurs in InGaAs layers, whereas the diffused charge carriers are captured in InAlAs layers [28,29]. Since it was shown that the most efficient terahertz radiation was generated in samples grown on substrates with an orientation different from the traditional (100) [20–22], to obtain the most efficient generation, the InGaAs / InAlAs heterostructure was grown straight on InP (111)A substrate. InAlAs layers significantly increase the resulting structure resistance. The resistance of the InGaAs / InAlAs sample on the InP (111)A substrate was 12.8 k Ω , which is significantly higher than the resistance of 30 Ω for all InGaAs samples on GaAs substrates. This made it possible to increase the bias voltage from 3.7 to 25 V without damaging the antenna and to raise the terahertz radiation power by almost 30 times. Since the reflections are present in the waveforms in Figure 5, the resulting spectra in Figure 6 are strongly modulated with a frequency inversely proportional to the delay between the main and reflected pulses. However, the main features of the antennas are clearly seen. The spectrum from the antenna on the LT-InGaAs/InAlAs heterostructure looks more pronounced and less “noisy” at high frequencies above 2 THz than from the LT-InGaAs antennas. Although the total spectral widths of all antennas on the logarithmic scale practically coincide in Figure 6, the total spectrum of the antenna on the heterostructure InGaAs/InAlAs is slightly wider than that of InGaAs. This issue needs a more detailed study using a wide range of radiation detectors to exclude the possible influence of the receiver on the measured spectrum.

For future research directions, we propose using atypically oriented substrates for the manufacture of antennas in order to obtain faster carrier dynamics, larger signals, and wider terahertz radiation spectra.

5. Conclusions

The characteristics of terahertz wave radiation from photoconductive antennas based on epitaxial films of low-temperature grown InGaAs with orientations of the crystallographic axes of the GaAs substrate (111)A and (100) were studied. It was found that the terahertz radiation power is almost four times higher for samples with the (111)A substrate orientation. The observed increase in the radiation power is associated with an increase in the number of anti-structural defects. THz radiation generated in the LT-InGaAs / InAlAs / InP (111)A heterostructure was 25 times higher than in the LT-InGaAs / GaAs (111)A antenna. The characteristic relaxation times of charge carriers were measured in LT-InGaAs samples on GaAs substrates with (111)A and (100) orientations, as well as in the LT-InGaAs/InAlAs/InP (111)A heterostructure. Obtained values are consistent with previously published data and qualitatively confirm the proposed explanation of the advantages of the non-standard orientation of the antenna substrate.

Author Contributions: Conceptualization, G.G.; MBE growth, E.K. and A.K.; Hall effect measurements, A.K.; PCA antenna, S.P.; pump-probe measurements, A.L. and K.K.; TDS measurements, A.L. and K.K.; measurement analysis, G.K.; data fitting, A.L.; writing and editing, K.K. and A.K. All authors have read and agreed to the published version of the manuscript.

Funding: This research was funded by RFBR, grants numbers 18-29-20101, 18-32-20207, 19-02-00598.

Acknowledgments: The authors thank D.S. Ponomarev for some helpful discussions, D.V. Lopaev for the help with experiments and I.S. Vasil’evskii, A.N. Vinichenko for help with MBE.

Conflicts of Interest: The authors declare no conflict of interest.

References

1. Vieweg, N.; Rettich, F.; Deninger, A.; Roehle, H.; Dietz, R.; Göbel, T.; Schell, M. Terahertz-time domain spectrometer with 90 dB peak dynamic range. *J. Infrared Milli Terahz Waves* **2014**, *35*, 823–832. [[CrossRef](#)]
2. Globisch, B.; Dietz, R.J.B.; Kohlhaas, R.B.; Göbel, T.; Schell, M.; Alcer, D.; Semtsiv, M.; Masselink, W.T. Iron doped InGaAs: Competitive THz emitters and detectors fabricated from the same photoconductor. *J. Appl. Phys.* **2017**, *121*, 053102. [[CrossRef](#)]

3. Castro-Camus, E.; Alfaro, M. Photoconductive devices for terahertz pulsed spectroscopy: A review. *Photon. Res.* **2016**, *4*, A36. [[CrossRef](#)]
4. Burford, N.M.; El-Shenawee, M.O. Review of terahertz photoconductive antenna technology. *Opt. Eng.* **2017**, *56*, 010901. [[CrossRef](#)]
5. Yardimci, N.T.; Jarrahi, M. Nanostructure-Enhanced Photoconductive Terahertz Emission and Detection. *Small J.* **2018**, *14*, 1802437. [[CrossRef](#)]
6. Lepeshov, S.; Gorodetsky, A.; Krasnok, A.; Rafailov, E.; Belov, P. Enhancement of terahertz photoconductive antenna operation by optical nanoantennas: Enhancement of terahertz photoconductive antenna operation by optical nanoantennas. *Laser Photonics Rev.* **2017**, *11*, 1600199. [[CrossRef](#)]
7. Yachmenev, A.E.; Lavrukhin, D.V.; Glinskiy, I.A.; Zenchenko, N.V.; Goncharov, Y.G.; Spektor, I.E.; Khabibullin, R.A.; Otsuji, T.; Ponomarev, D.S. Metallic and dielectric metasurfaces in photoconductive terahertz devices: A review. *Opt. Eng.* **2019**, *59*, 061608. [[CrossRef](#)]
8. Petrov, B.; Fekecs, A.; Sarra-Bournet, C.; Ares, R.; Morris, D. Terahertz Emitters and Detectors Made on High-Resistivity InGaAsP:Fe Photoconductors. *IEEE Trans. THz Sci. Technol.* **2016**, *6*, 1–7. [[CrossRef](#)]
9. Suzuki, M.; Tonouchi, M. Fe-implanted InGaAs terahertz emitters for 1.56 μm wavelength excitation. *Appl. Phys. Lett.* **2005**, *86*, 051104. [[CrossRef](#)]
10. Kohlhaas, R.B.; Breuer, S.; Nellen, S.; Liebermeister, L.; Schell, M.; Semtsiv, M.P.; Masselink, W.T.; Globisch, B. Photoconductive terahertz detectors with 105 dB peak dynamic range made of rhodium doped InGaAs. *Appl. Phys. Lett.* **2019**, *114*, 221103. [[CrossRef](#)]
11. Yardimci, N.T.; Lu, H.; Jarrahi, M. High power telecommunication-compatible photoconductive terahertz emitters based on plasmonic nano-antenna arrays. *Appl. Phys. Lett.* **2016**, *109*, 191103. [[CrossRef](#)] [[PubMed](#)]
12. Nandi, U.; Norman, J.C.; Gossard, A.C.; Lu, H.; Preu, S. 1550-nm Driven ErAs:In(Al)GaAs Photoconductor-Based Terahertz Time Domain System with 6.5 THz Bandwidth. *J. Infrared Milli Terahz Waves* **2018**, *39*, 340–348. [[CrossRef](#)]
13. Künzel, H.; Böttcher, J.; Gibis, R.; Urmann, G. Material properties of GaInAs grown on InP by low-temperature molecular beam epitaxy. *Appl. Phys. Lett.* **1992**, *61*, 1347–1349. [[CrossRef](#)]
14. Metzger, R.A. Structural and electrical properties of low temperature GaInAs. *J. Vac. Sci. Technol. B* **1993**, *11*, 798. [[CrossRef](#)]
15. Grandidier, B.; Chen, H.; Feenstra, R.M.; McInturff, D.T.; Juodawlkis, P.W.; Ralph, S.E. Scanning tunneling microscopy and spectroscopy of arsenic antisites in low temperature grown InGaAs. *Appl. Phys. Lett.* **1999**, *74*, 1439–1441. [[CrossRef](#)]
16. Baker, C.; Gregory, I.S.; Tribe, W.R.; Bradley, I.V.; Evans, M.J.; Linfield, E.H.; Missous, M. Highly resistive annealed low-temperature-grown InGaAs with sub-500fs carrier lifetimes. *Appl. Phys. Lett.* **2004**, *85*, 4965–4967. [[CrossRef](#)]
17. Dietz, R.J.B.; Globisch, B.; Roehle, H.; Stanze, D.; Göbel, T.; Schell, M. Influence and adjustment of carrier lifetimes in InGaAs/InAlAs photoconductive pulsed terahertz detectors: 6 THz bandwidth and 90dB dynamic range. *Opt. Express* **2014**, *22*, 19411. [[CrossRef](#)]
18. Ponomarev, D.S.; Gorodetsky, A.; Yachmenev, A.E.; Pushkarev, S.S.; Khabibullin, R.A.; Grekhov, M.M.; Zaytsev, K.I.; Khusyainov, D.I.; Buryakov, A.M.; Mishina, E.D. Enhanced terahertz emission from strain-induced InGaAs/InAlAs superlattices. *J. Appl. Phys.* **2019**, *125*, 151605. [[CrossRef](#)]
19. Kuenzel, H.; Biermann, K.; Nickel, D.; Elsaesser, T. Low-temperature MBE growth and characteristics of InP-based AlInAs/GaInAs MQW structures. *J. Cryst. Growth* **2001**, *227–228*, 284–288. [[CrossRef](#)]
20. Kuznetsov, K.A.; Galiev, G.B.; Kitaeva, G.K.; Kornienko, V.V.; Klimov, E.A.; Klochkov, A.N.; Leontyev, A.A.; Pushkarev, S.S.; Malrsev, P.P. Photoconductive antennas based on epitaxial films In_{0.5}Ga_{0.5}As on GaAs (111)A and (100)A substrates with a metamorphic buffer. *Laser Phys. Lett.* **2018**, *15*, 076201. [[CrossRef](#)]
21. Galiev, G.B.; Grekhov, M.M.; Kitaeva, G.K.; Klimov, E.A.; Klochkov, A.N.; Kolentsova, O.S.; Kornienko, V.V.; Kuznetsov, K.A.; Maltsev, P.P.; Pushkarev, S.S. Terahertz-radiation generation in low-temperature InGaAs epitaxial films on (100) and (411) InP substrates. *Semiconductors* **2017**, *51*, 310–317. [[CrossRef](#)]
22. Galiev, G.B.; Pushkarev, S.S.; Buriakov, A.M.; Bilyk, V.R.; Mishina, E.D.; Klimov, E.A.; Vasil'evskii, I.S.; Maltsev, P.P. Terahertz-radiation generation and detection in low-temperature-grown GaAs epitaxial films on GaAs (100) and (111)A substrates. *Semiconductors* **2017**, *51*, 503–508. [[CrossRef](#)]
23. Bacher, F.R.; Blakemore, J.S.; Ebner, J.T.; Arthur, J.R. Optical-absorption coefficient of InGaAs/InP. *Phys. Rev. B* **1988**, *37*, 2551–2557. [[CrossRef](#)] [[PubMed](#)]

24. Zielinski, E.; Schweizer, H.; Streubel, K.; Eisele, H.; Weimann, G. Excitonic transitions and exciton damping processes in InGaAs/InP. *J. Appl. Phys.* **1986**, *59*, 2196–2204. [[CrossRef](#)]
25. Globisch, B.; Dietz, R.J.B.; Stanze, D.; Gobel, T.; Schell, M. Carrier dynamics in Beryllium doped low-temperature-grown InGaAs/InAlAs. *Appl. Phys. Lett.* **2014**, *104*, 172103-1-4. [[CrossRef](#)]
26. Shockley, W.; Read, W.T. Statistics of the Recombinations of Holes and Electrons. *Phys. Rev.* **1952**, *87*, 835–842. [[CrossRef](#)]
27. Auston, D.H.; Cheung, K.P.; Smith, P.R. Picosecond photoconducting Hertzian dipoles. *Phys. Lett.* **1984**, *45*, 284–286. [[CrossRef](#)]
28. Sartorius, B.; Roehle, H.; Kunzel, H.; Boettcher, J.; Schlak, M.; Stanze, D.; Venghaus, H.; Schell, M. All-fiber terahertz time-domain spectrometer operating at 1.5 μm telecom wavelengths. *Opt. Express* **2008**, *16*, 9565–9570. [[CrossRef](#)]
29. Dietz, R.J.B.; Globisch, B.; Gerhard, M.; Velauthapillai, A.; Stanze, D.; Roehle, H.; Koch, M.; Gobel, T.; Schell, M. 64 μW pulsed terahertz emission from growth optimized InGaAs/InAlAs heterostructures with separated photoconductive and trapping regions. *Appl. Phys. Lett.* **2013**, *103*, 061103-1-4. [[CrossRef](#)]



© 2020 by the authors. Licensee MDPI, Basel, Switzerland. This article is an open access article distributed under the terms and conditions of the Creative Commons Attribution (CC BY) license (<http://creativecommons.org/licenses/by/4.0/>).